Journal of Nanosciences: Current Research

Parvathya and Venatramanb, J Nanosci Curr Res 2017, 2:1
DOI: 10.4172/2572-0813.1000111

Research Article Open Access

Invitro Antibacterial and Anticancer Potential of CeO_2 Nanoparticles Prepared by Co-precipitation and Green Synthesis Method

Parvathya S[1*] and Venkatramanb BR[2]

[1]*Department of Chemistry, Government Arts College (Autonomous), Salem, Tamil Nadu, India*

[2]*Department of Chemistry, Periyar E.V.R. College, Tiruchirappalli, Tamil Nadu, India*

[*]**Corresponding author:** D. S Parvathya, Department of Chemistr, Government Arts College, Tamil Nadu, India, Tel: +919629019582; E-mail: chemparuvenkat@gmail.com

Received date: May 24, 2017; **Accepted date:** June 12, 2017; **Published date:** June 19, 2017

Abstract

Cerium oxide nanoparticles (CeO_2 NPs) were synthesized through chemical (co-precipitation method) (C-CeO_2 NPs) and green synthetic route (*A. indica* leaf extract) (G-CeO_2 NPs) and comparative studies were also carried out in the first time. From the XRD Pattern of C-CeO_2 and G-CeO_2 NPs revealed that both were in cubic phase. The morphological and elemental compositions were identified by FESEM, TEM and EDAX spectra. The optical characterizations were carried out using UV-Visible and Photoluminescence spectral analysis. Further the FT-IR and FT-Raman analysis were also confirmed to formation of CeO_2 nanoparticles. The oxidation states of the elements Ce (3d), C (1s) and O (1s) were confirmed by XPS studies. The green synthesized CeO_2 NPs possessed a higher antibacterial activity than chemical CeO_2 NPs. The cytotoxic effect of C-CeO_2 and G-CeO_2 NPs were analyzed in cultured (A549) human lung cancer cell line.

Keywords: C-CeO_2 NPs; G-CeO_2; Flake morphology; Antibacterial activity; Anticancer activity

Introduction

Cerium oxide is a semiconductor with wide band gap energy (3.19 eV) and large exciton binding energy. However, the CeO_2 NPs is used in extensive applications such as sunscreens, solid electrolytes, solar cells, fuel cells, phosphor/luminescence, photocatalysis, and sensors and mainly in the biomedical industry due to their strong antioxidant properties etc. These potential applications involve its potential redox chemistry containing Ce^{3+}/Ce^{4+} and the single useful absorption/excitation energy bands associated with its electronic structure [1-3].

Ceria is the only compounds are the highly used rare earth compounds possessing wide applications in industrial and commercial products. It is also an excellent absorber of ultraviolet radiation and can be used as an alternative for zinc oxide or titanium oxide nanoparticles in cosmetics.

The green chemistry approaches to the development in phytosynthesis of metal and metal oxide NPs. Green synthesis method offers a plenty of advantages such as cost-effectiveness, large-scale commercial production and pharmaceutical applications. The CeO_2 NPs is a unique nanomaterial because it exhibit anti-inflammatory properties. CeO_2 NPs possessing superoxide-dismutase like activity prevent cardiovascular myopathy and provide radioprotection to normal cells from radiation [4-7]. In literature, Reddy Yadav et al. reported the watermelon juice extract mediated synthesis of CeO_2 NPs are degrading the methylene blue dye at 98% for UV irradiations and also studied the antibacterial activity against to bacterial strains K. aerogenes and S. aureus [8], Arumugam et al. Gloriosa superba L. leaf extract with CeO_2 were examined under Gram positive (G+) and Gram negative (G-) bacteria and were relatively more susceptible to the CeO_2 NPs than Gram negative (G-) bacteria [9].

Azadirachta indica, also known as Neem, Nimtree, and Indian Lilac is a tree in the mahogany family Meliaceae. The neem trees have been used in India for over two millennia for their medicinal properties. Neem products are believed by Siddha and Ayurvedic practitioners to be anthelmintic, antifungal, antidiabetic, antibacterial, antiviral, contraceptive and sedative. This is a major source component in Siddha, Ayurvedic and Unani medicines and is particularly prescribed for skin diseases [10]. Neem oil is also used for healthy hair, to improve liver function, detoxify the blood, and balance blood sugar levels. The neem leaves have also been used to treat skin diseases like eczema, psoriasis, etc.

Henceforth the present work, we synthesize CeO_2 NPs through chemical pathway (co-precipitation method) and an environmentally benign green pathway using *A. indica* leaf extract and characterize the materials with suitable analytical tools. Further the efficiency of the materials studied as a function of antibacterial and anticancer against some G+ and G- staining bacteria and human lung cancer cell line (A549) results were compared.

Materials and Methods

The materials used in this experiment are purchased from the merck with high purity and used as such without further purification.

Chemical synthesis CeO_2 NPs

Cerium nitrate (0.1 M) and NaOH (0.8 M) were dissolved in 100 ml of double distilled water separately. Then add sodium hydroxide solution to cerium nitrate solution as drop by drop with constant stirring. The resultant solution precipitated as violet in colour and the stirring continued upto 5 h. Thereafter, the precipitate was washed several times with double distilled water and followed by ethanol. Finally, the precipitate was dried at 120°C and annealed at 400°C for 5

h to get nanoflake structure. Thus, CeO_2 nanopowder was obtained and labeled as C-CeO_2.

Green synthesis CeO_2 NPs

The 10 g of finely divided leaves of *Azadirachta indica* were added to 100 mL of double distilled water and boiled at 50-60°C for 15 min. The solution was filtered through Whatmann No. 1 filter paper and the clear filtrate was collected and which was carry for further usage. Thereafter, add certain quantity of 0.1 M solution of cerium nitrate to 100 mL of *A. indica* leaf extract with constant stirring at 80°C for 5 h. Initially brown precipitate was formed and then it is become a yellowish brown in color on continuous stirring. Further the precipitate was washed with water and followed by ethanol. The precipitate was annealed at 400°C for 5 h to get spherical NPs and labeled as G-CeO_2. The schematic diagram for the formation of CeO_2 NPs using *Azadirachta indica* leaf extract is shown in Figure 1.

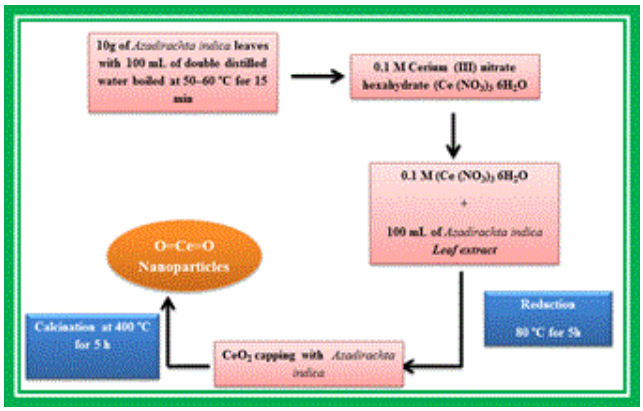

Figure 1: A schematic diagram for the formation of CeO_2 NPs using *Azadirachta indica* leaf extract.

Antibacterial assay

The antibacterial activity of the C-CeO_2 and G-CeO_2 NPs were carried out by the well diffusion method against the bacterial strains of *(K. pneumonia (1), S. aureus (2), S. dysenteriae (3), E. coli (4), P. aeruginosa (5), S. pneumonia (6) and P. vulgaris (7)*) on Mueller hinton agar, according to the Clinical and Laboratory Standards Institute (CLSI) [11]. The media plate's Mueller hinton agar (MHA) was streaked with bacteria 2-3 times by rotating the plate at 60˚ angles for each streak to ensure the homogeneous distribution of the inoculums. After inoculation, discs (6 mm Hi-Media) loaded 1.5 mg/ml and 1.75 mg/ml, of the test samples were placed on the bacteria-seeded well plates using micropipettes. The plates were then incubated at 37˚C for 24 h. The inhibition zone around the well was measured and recorded. Amoxicillin (Hi-Media) was used as the positive controls against *(K. pneumonia (1), S. aureus (2), S. dysenteriae (3), E. coli (4), P. aeruginosa (5), S. pneumonia (6) and P. vulgaris (7))* bacteria respectively. The positive controls results were as compared to that of the efficacy of the test C-CeO_2 and G-CeO_2 samples.

Cell culture

The A549 human lung cancer cell line was obtained from National Center for Cell Science (NCCS), Pune, India. The cells were cultured in DMEM high glucose medium (Sigma-Aldrich, USA), supplemented with 10% fetal bovine serum (Gibco), and 20 mL of penicillin as antibiotics (Gibco), in 96 well culture plates, at 37°C in a humidified atmosphere of 5% CO_2 in a CO_2 incubator (Thermo scientific, USA). All experiments were performed using cells from passage 15 or less.

Cell viability assay

The C-CeO_2 and G-CeO_2 NPs were suspended in dimethyl sulfoxide (DMSO) to make a stock. These stock solutions were diluted separately with media to get various concentrations of the complex. Two hundred micro liters of these samples were added to wells containing 5×10^3 A549 cells per well. DMSO solution was used as the solvent control. After 24 h, 20 µl of 3-(4, 5-di-methylthiazol-2-yl)-2, 5-diphenyl-2H-tetrazolium bromide MTT solution (5 mg/ml in PBS) was added to each well and the plate was covered with aluminum foil and incubated for 4 h at 37°C [12].

The purple formazan outcome was dismissed by adding 100 µl of dimethyl sulfoxide to each well. The absorbance was recorded at 570 nm (measurement) and 630 nm (reference) using a 96-well plate reader (Bio-Rad, iMark, USA). Data were possessed for three replicates each and used to calculate the respective mean. The percentage inhibition was calculated from the data using the formula:

$$= \frac{mean\,OD\,of\,untreated\,cells\,(control) - mean\,OD\,of\,treated\,cells}{mean\,OD\,ofuntreated\,cells\,(control)} x\ 100$$

Acridine orange (AO) and Ethidium bromide (EB) staining

Apoptotic morphology was investigated by AO/EB double staining method as described by Spector et al. with some modifications [13]. Briefly, the cells treated with IC50 Concentration of C-CeO_2 and G-CeO_2 for a day. After incubation, the cells were harvested and washed with cold PBS. Cell pellets were diluted with PBS to a concentration of 5×10^5 cells/mL and mixed with 25 µl of AO/EB solution (3.8 µM of AO and 2.5 µM of EB in PBS) on clean microscope slide and immediately examined under fluorescent microscope (Carl Zeiss, Axioscope 2 plus) with UV filter (450-490 nm).

Characterization techniques

The CeO_2 NPs were characterized by X-ray diffractometer (model: X'PERT PRO PAN alytical). The diffraction patterns were recorded in the range of 200-800 for the CeO_2 NPs samples, where the monochromatic wavelength of 1.54 Å was used. The XPS measurements were performed with an XPS instrument (Carl Zeiss) equipment. The spectra were at a pressure using an ultra high vacuum with Al Kα excitation at 250 W.

The samples were analyzed by Field Emission Scanning Electron Microscopy (Carl Zeiss Ultra 55 FESEM) with EDAX (model: Inca). TEM analyses were carried out by the instrument Philips CM 200 model operated at an accelerating voltage of 20-200 kv Resolution: 2.4 Å. The FT-IR spectra were recorded in the range of 400-4000 cm^{-1} by using a Perkin-Elmer spectrometer. The absorption spectra of CeO_2 NPs were studied in the range between 200 and 800 nm by Lambda 35 spectrometer. Photoluminescence spectra were measured using Cary Eclipse spectrometer.

Results and Discussion

X-ray diffraction studies

The XRD patterns of C-CeO_2 and G-CeO_2 NPs are shown in Figure 2. The diffraction pattern corresponds to the cubic phase of CeO_2 [14]. The XRD peaks are located at angles (2θ) of (28.70, 33.01, 47.60, 56.04 and 76.87) and (28.53, 33.00, 47.51, 56.61 and 76.34) corresponding to (111), (200), (220), (311), (222) and (331) planes of the both CeO_2 NPs respectively. The face-center cubic phase of CeO_2 NPs exactly matches JCPDS data card no: 34-0394. The G-CeO_2 NPs are more crystalline nature as compared to C-CeO_2. More crystallinity nature of G-CeO_2 NPs is due to the presence of many organic components involved in the NPs formation [15].

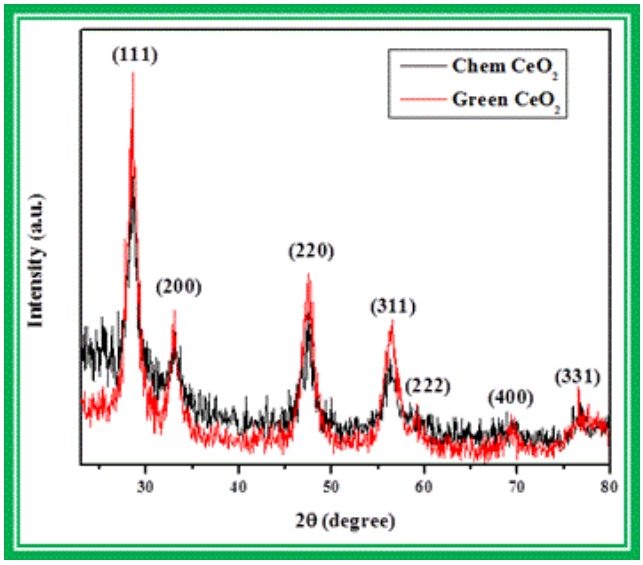

Figure 2: X-ray powder diffraction patterns of the C-CeO_2 and G-CeO_2 NPs. X-ray photoelectron spectroscopic studies.

The lattice constant 'a' of CeO_2 can be calculated by using the relation,

$$\frac{1}{d^2} = \left(\frac{h^2+k^2+l^2}{a^2}\right)$$ The lattice constant 'a' is obtained through the relation $a = \sqrt{d^2(h^2+k^2+l^2)}$.

The calculated 'a' values are 5.3865Å and 5.4108 Å for C-CeO_2 and G-CeO_2 NPs respectively. The unit cell volume can be calculated using the relation; V= a3. The unit cell volume is found to be 156.288 Å3 and 157.464 Å3 for both CeO_2 NPs.

The average crystallite size D of the sample is calculated after appropriate background corrections from X-ray line broadening of the diffraction peaks using Debye-Scherrer's formula.

$$\text{Average crystallite size } D = \frac{0.9\ \lambda}{\beta cos\ \theta}$$

where λ is the wavelength of X-ray used (1.5405 A), β is the angular peak width at half maximum in radians and θ is the Bragg's diffraction angle. The average crystallite sizes are 11 nm and 8 nm for C-CeO_2 and G-CeO_2 NPs respectively. From the above result revealed that the green synthesized CeO_2 more easily reduced into NPs without much effort and also it might be exhibit better antibacterial activity.

The XPS results show that the indexed peaks correspond to the C (1s), O (1s), and Ce (3d) for CeO_2 NPs. The C (1s) signals are most likely due to remaining trace amount of plant extract.

The Ce (3d) states divided into seven signals in the Gaussian fitting are shown in Figure 3. Binding energy of C-CeO_2 and G-CeO_2 NPs has seven bands (881.92, 886.19, 891.62, 902.59, 907.75, 910.91 and 919.26eV) and (883.43, 890.07, 898.16, 901.27, 907.99 and 919.98 eV) for Ce (3d) states respectively. The BE of Ce 3d state values are observed at 898.16 eV for Ce4+ 3d5/2 and (919.26 and 919.98 eV) for Ce4+ 3d3/2 for C-CeO_2 and G-CeO_2 NPs.

The oxidation state of Ce3+ 3d5/2 and Ce3+ 3d3/2 are specified at (902.59 eV and 881.92 eV) and (901.27 eV and 883.43 eV) for both CeO_2 NPs. Four additional satellite peaks are (886.19 eV and 891.62 eV) and (890.07 eV) for Ce3+ 3d5/2 and (907.75 eV and 910.91 eV) and 907.99 eV for Ce^{3+} 3d3/2 respectively. This satellite peaks are shake-up and shake-down for Ce3+ 3d states [9,16]. Comparison of chemical and green synthesized CeO_2 NPs binding energy and FWHM values are given in Table 1.

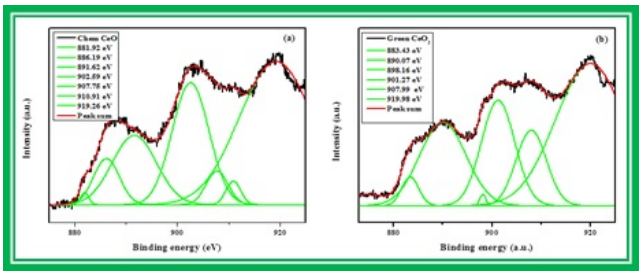

Figure 3: XPS spectra of the Ce (3d) of (a) C-CeO_2 NPs and (b) G-CeO_2 NPs.

Chem-CeO_2 eV	Chem-CeO_2 (FWHM)	Green-CeO_2 eV	Green-CeO_2 (FWHM)
881.92	1.66365	883.43684	3.54475
886.19	5.08273	-	-
891.62	8.69749	890.07919	9.43212
898.16	8.69749	898.16628	1.26095
902.59	7.19858	901.27919	6.79635
907.75	4.35778	907.99918	6.18185
910.91	2.93668	-	-
919.26	14.49466	919.98999	14.18896

Table 1: Comparison of chemical and green synthesized CeO_2 NPs binding energy and FWHM values.

The C (1s) signal splits three symmetric peaks (284.01 eV, 285.24 eV and 287.76 eV) (284.66 eV, 288.55 eV and 294.41 eV) for C-CeO_2 and G-CeO_2 NPs in the Gaussian fitting are shown in Figure 4. The first C 1s signal center at 284.01 eV and 284.66 eV are ascribed to C-C state for both CeO_2 NPs.

The oxidized carbon peak is C-OH at 285.24 eV for CeO_2 NPs. Finally O-C=O peaks are observed at 287.76 eV and (288.55 eV and 294.41 eV) for C-CeO_2 and G-CeO_2 NPs respectively.

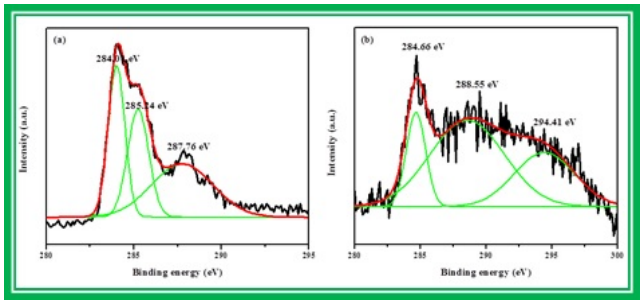

Figure 4: XPS spectra of the C (1s) of (a) CeO_2 NPs and (b) GCeO_2 NPs.

Figure 5 indicates an oxygen O (1s) asymmetric signals divided into three and four symmetrical signals for C-CeO_2 and G-CeO_2 NPs. The BE of O (1s) values are observed at (528.79 eV, 532.40 eV and 535.60 eV) and (529.25 eV, 531.35 eV, 534.58 eV and 538.86 eV) for both CeO_2 NPs respectively.

The first O (1s) signal at 528.79 eV and 529.25 eV are attributed to O_2- ions surrounded by Ce^{4+} ions, which is corresponds to the Ce-O bond in CeO_2 NPs. The second O (1s) signals center at 532.40 eV and 531.35 eV can be ascribed to the O_2- ions in the Ce-O bonds and it is due to the Ce3+ ion state in C-CeO_2 and G-CeO_2 NPs. Third O (1s) signals located at 535.47 eV and (534.58 eV and 538.86 eV) are not related to the presence of either Ce^{3+} or Ce^{4+}. This is due to the OH on the surface of the CeO_2 NPs.

Transmission electron microscopic studies

TEM morphology of C-CeO_2 and G-CeO_2 NPs are shown in Figure 7. Figures 7a and 7b shows that the C-CeO_2 NPs are uniformly ascribed nanoflake morphology. Figures 7d and 7e are attributed to G-CeO_2 NPs in the uniform spherical shape morphology with well-organized crystalinity. Further, the TEM micrographs clearly show that both the particles are uniformly distributed with average size range between 5-6 nm.

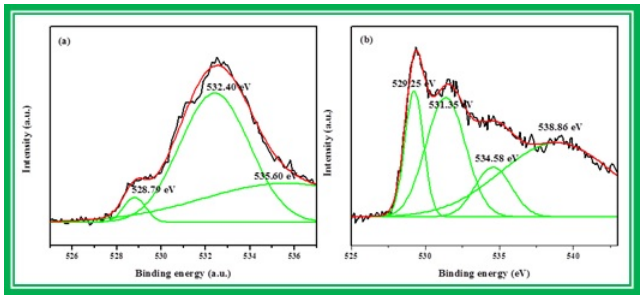

Figure 5: XPS spectra of the O (1s) of (a) C-CeO_2 NPs and (b) G-CeO_2 NPs.

FESEM analysis

The surface morphology of C-CeO_2 and G-CeO_2 NPs are shown in Figure 6. The entire FESEM image clearly shows that the average sizes of the NPs are in nanometer scale. The C-CeO_2 NPs are formed nano flake like structure Figure 6.

Thickness of the flake is 5-6 nm. However, CeO_2 using *A. indica* leaf extract NPs are formed spherical structure with even grain boundaries formed.

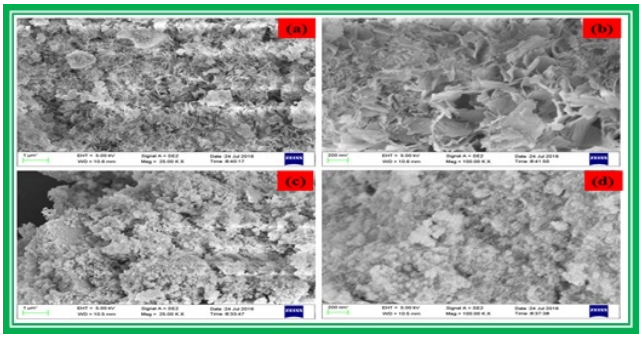

Figure 6: FESEM image of low and high magnification of the (a-b) C-CeO_2 NPs and (c-d) G-CeO_2 NPs.

The SAED patterns are also evidenced with the above illustrations which are shown in Figures 7c and 7f. The reflection peaks are (1 1 1), (2 0 0), (2 2 0), (3 1 1), (2 2 2), (40 0), (3 3 1) and (4 2 0) of face center cubic structure of CeO_2 NPs. From the SAED pattern spotty rings shows small polycrystalline nature is observed for C-CeO_2 NPs and good crystalline nature are observed for Green synthesized CeO_2 NPs and this is good agreement with XRD result.

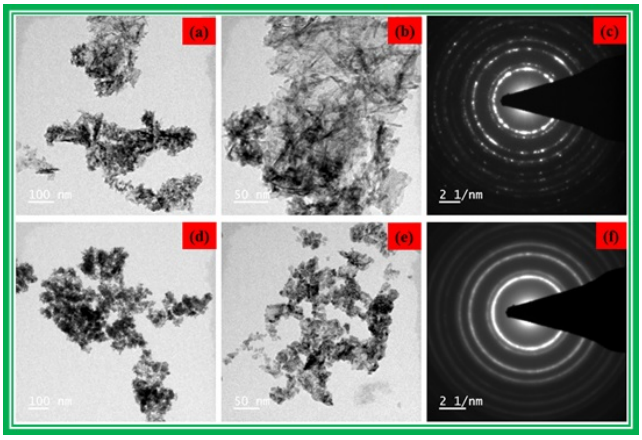

Figure 7: TEM images at different magnifications (a-b) C-CeO_2 NPs, (c) SAED pattern of C-CeO_2 NPs, (d-e) G-CeO_2 NPs and (f) SAED pattern of G-CeO_2 NPs.

EDX analysis

In order to find out the elemental composition of the C-CeO_2 and G-CeO_2 NPs, EDX spectra recorded which are shown in Figure 8. The EDX Spectra (Figure 8a) clearly indicated that only Ce and O were

composed in the weight percentage of 60 and 40% for C-CeO_2 NPs. The EDX spectra of G-CeO_2 NPs are composed of Ce and O in addition to C, which is from plant extract. The elemental composition of Ce, O and C are 15.82%, 64.03% and 20.15% respectively.

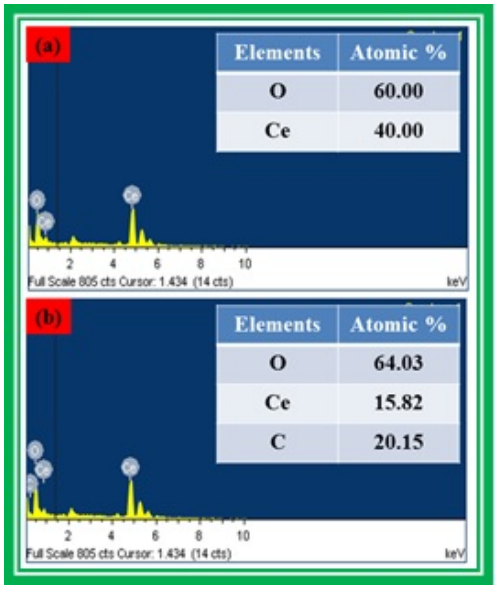

Figure 8: EDAX spectra of the (a) C-CeO_2 and (b) G-CeO_2 NPs.

FT-IR spectroscopic analysis

The FTIR spectra of C-CeO_2 and G-CeO_2 NPs are shown in Figure 9. In literature, the broad absorption in the frequency band 3750-3000 cm^{-1} are assigned to O-H stretching from residual alcohols, water and Ce-OH [9]. From the FTIR result, the absorption peaks at 3404 and 3389 cm^{-1} are attributed to the O-H mode for C-CeO_2 and G-CeO_2 NPs respectively.

The peaks at 2860 and 2950 cm^{-1} are due to symmetric and asymmetric stretching of C-H bonds [17]. However, symmetric and asymmetric C-H stretching bands observed at 2855 cm^{-1} and 2925 cm^{-1} for both CeO_2 NPs. The absorption bands are caused by the vibration in CO_{32}^{-} between 400 and 1800 cm^{1} on the metallic cation groups.

In FT-IR result, C=O peaks found at 1703 and 1707 cm^{-1} for C-CeO_2 and G-CeO_2 NPs respectively. The band at 1620 and 1603 cm^{-1} corresponds to the bending of H-O-H, which is partly overlapping the O-C-O stretching bands for C-CeO_2 and G-CeO_2 NPs respectively. The C=O stretching observed at (1545 and 1384 cm^{-1}) and (1505 and 1384 cm^{-1}) for both CeO_2 NPs. In the present work, the Ce-O stretching vibration are observed at (960 and 982 cm^{-1}), (854 and 840 cm^{-1}), (724 and 702 cm^{-1}), (494 and 537 cm^{-1}) and (411 and 429 cm^{-1}) for C-CeO_2 and G-CeO_2 NPs respectively.

Raman spectroscopic analysis

Raman is a common vibrational spectroscopic technique for evaluating the molecular motion of the materials and providing information about the structure and symmetry of the molecule. The Raman spectra of C-CeO_2 and G-CeO_2 NPs are shown in Figure 10. In early literature, Raman active triply degenerated 2 modes are observed at 458, 462 and 467 cm^{-1} for SDS, PEG, and CTAB coated CeO_2 samples [18].

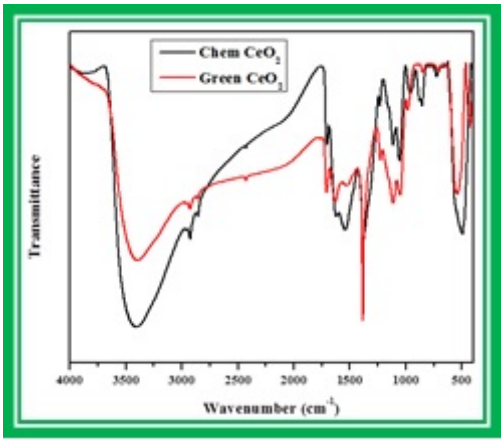

Figure 9: FT-IR spectra of the C-CeO_2 and G-CeO_2 NPs.

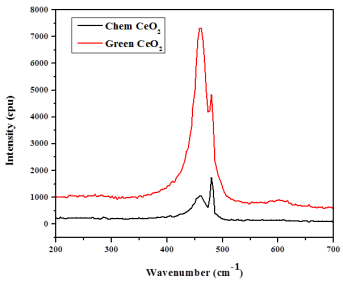

Figure 10: Raman spectra of the C-CeO_2 and G-CeO_2.

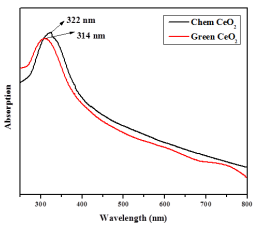

Figure 11: UV–visible spectra of the C-CeO_2 and G-CeO_2 NPs.

In present work, the C-CeO_2 and G-CeO_2 NPs are located at 459 and 462 cm^{-1}, this is due to the triply degenerate F2g Raman active

mode of fluorite-type cubic structure i.e., asymmetric breathing mode of the oxygen atoms around the cerium ions [19,20].

UV-Vis spectroscopy studies

The UV-Vis optical absorption spectra of C-CeO_2 and G-CeO_2 NPs are shown in Figure 11. The absorption peaks are found at 322 nm and 314 nm for C-CeO_2 and G-CeO_2 NPs respectively, and it is due to the photo excitation of electrons from the valence band to the conduction band.

The G-CeO_2 NPs wavelength is decreased as compared to the C-CeO_2 NPs wavelength. This indicates that the band gaps of G-CeO_2 NPs are increased with the *A. indica* leaf extract capped with CeO_2 NPs.

The relation between the absorption coefficients α and the incident photon energy hυ can be written as

$\alpha h\upsilon = A\left(h\upsilon - E_g\right)^n$ Where Eg is the optical bandgap, A is the constant and the exponent n depends on the type of transition. The n = 1/2 for allowed direct transition, 2 for allowed indirect transition 3/2 and 3 for forbidden direct and indirect transitions respectively.

Considering direct and indirect band transition in CeO_2 NPs, a plot between (αhυ)2 vs. photon energy hυ and extrapolating the linear portion of the absorption edge to find the intercept with energy axis are shown in Figure 12. The estimated direct and indirect band gaps of the C-CeO_2 and G-CeO_2 NPs samples are observed at (2.4 eV and 2.8 eV) and (2.45 eV and 2.95 eV) respectively.

The many organic components are capped with forming the G-CeO_2 NPs and these organic components capping increases the band gap, this may be increase in the optical band gap for G-CeO_2 NPs. The quantum confinement effect is considered and when the particle is down to a few nanometers [21].

Since the fundamental band gap is mainly deduced by quantum size effect and when the particle size is equal to 3-5 nm. The quantum size effect in the present CeO_2 NPs with particle size of 5 nm may be ruled out and the charge transition of Ce ion (Ce^{3+}-Ce^{4+}) may play an important role for the increase in the band gap of present CeO_2 NPs using *A. indica* leaf extract.

Photoluminescence spectroscopic studies

The photoluminescence spectra of the synthesized C-CeO_2 and G-CeO_2 NPs were recorded with the excited wavelength of 325 nm. The PL emission peaks are observed for C-CeO_2 and G-CeO_2 NPs, from the very short wavelength of 350 nm to the longer wavelength of 550 nm.

A good fit with eight peaks using a Gaussian function was obtained. The PL spectra of the C-CeO_2 and G-CeO_2 samples values are (360, 376, 389, 411, 444, 460, 490, and 521 nm) and (361, 378, 391, 412, 444, 460, 490, and 522 nm) are shown in Figure 13.

The three near band edge emission are observed at (360 nm, 376 nm and 389 nm) and (361 nm, 378 nm and 391 nm) for C-CeO_2 and G-CeO_2 NPs respectively, this NBE emission is attributed to a band-to-band recombination process, possibly involving localized or free exciton [22]. The violet emission band centered at 411 nm and 412 nm for both CeO_2 NPs are attributed to defect states existing extensively between the Ce 4f state and O 2p valence band [23].

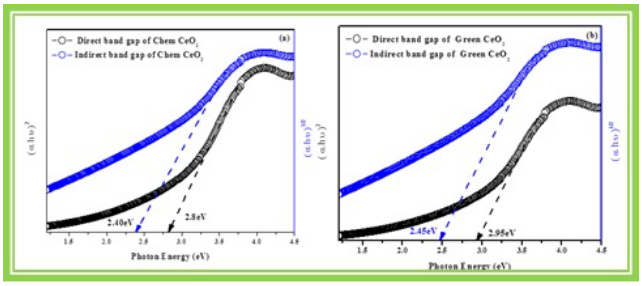

Figure 12: Photon energy level direct and indirect band gap of (a) C-CeO_2 and (b) G-CeO_2 NPs.

The two blue emissions values are observed at 444 nm and 460 nm for C-CeO_2 and G-CeO_2 NPs and this is due to localization of the energy levels between the Ce 4f band and the O 2p. The blue-green emission located at 490 nm is possibly due to surface defects in the C-CeO_2 and G-CeO_2 NPs respectively [9,24]. The green emission peaks observed at 521 nm and 522 nm are due to the low density of oxygen vacancies.

In PL spectra, red shift observed for G-CeO_2 NPs emission values as compared to that of the CeO_2 NPs emission values. This is due to the formation of more organic impurity levels.

The defect state is localized in between the Ce 4f and O 2p levels, leading to a red shift. These changes in the emissions are confirmed that the *A. indica* leaf extract reduced to forming the CeO_2 NPs.

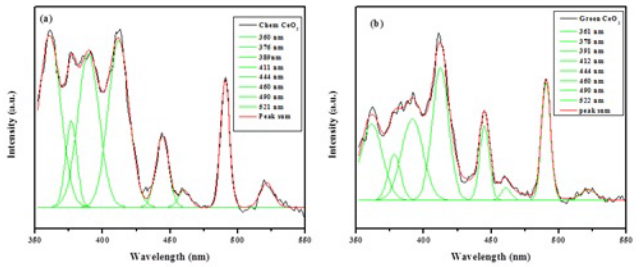

Figure 13: Photoluminescence emission spectra of the (a) C-CeO_2 and (b) G-CeO_2 NPs.

Antibacterial studies

In the present work, C-CeO_2 and G-CeO_2 NPs are tested against Gram-positive bacteria *(S. aureus and S. pneumoniae)* and Gram-negative bacteria *(E. coli, P. aeruginosa, P. vulgaris, K. pneumonia and S. dysenteriae)* studied well diffusion method are shown in Figure 14. Figure 15 shows the size of the zone of inhibition and antibacterial activity formed around each well concentration (1.5 mg/ml and 1.75 mg/ml) of C-CeO_2 and G-CeO_2 NPs loaded with test samples.

The inhibition zone of G-CeO_2 NPs possesses more antibacterial activity than C-CeO_2 NPs. The antibacterial activity of NPs may either directly interact with the microbial cells or to produce secondary products that cause damage. There are several mechanisms behind the antibacterial activity of metal oxide nano materials.

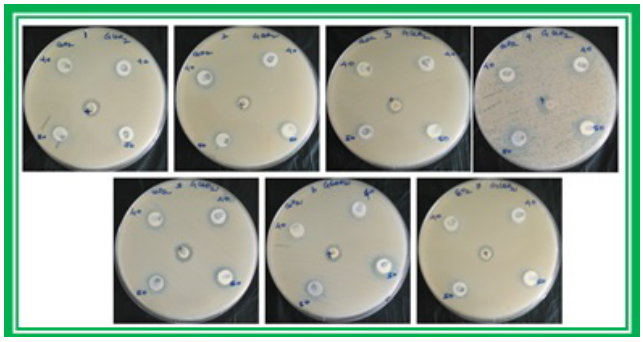

Figure 14: The progressive antibacterial activity of the C-CeO_2 and G-CeO_2 NPs against Gram-positive *(S. aureus (2) and S. pneumonia (6)) and Gram-negative (E. coli (4), P. aeruginosa (5), P. vulgaris (7), K. pneumonia (1) and S. dysenteriae (3)).*

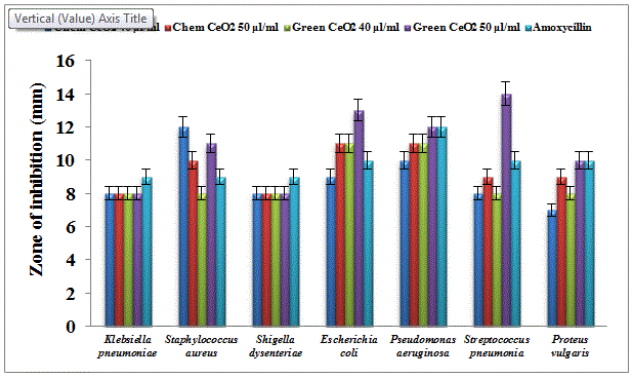

Figure 15: The size of the zone of inhibition formed around each disc, loaded with test samples, indicating the antibacterial activity towards Gram-positive *(S. aureus (2) and S. pneumonia (6)) and Gram-negative (E. coli (4), P. aeruginosa (5), P. vulgaris (7), K. pneumonia (1) and S. dysenteriae (3)) for the (C-CeO2 and G-CeO2 NPs).*

The antibacterial mechanism, the CeO_2 NPs can be active by UV light, to increase electron-hole pairs.

These holes split the H_2O molecule from the suspension of CeO_2 into hydroxyl radical (OH^-) and hydrogen ion (H^+). Dissolved oxygen molecules are converted to superoxide radical anions (O_2^-) which react with hydrogen ion (H^+) to produce HO_2^- radical.

These hydroxyl radicals on collision with electrons produce hydrogen peroxide. HO_2- anions which are react with hydrogen to produce H_2O_2 molecules. The generated H_2O_2 molecules can penetrate the cell membrane and arrest the biological process in the bacteria.

The negatively charged particles of hydroxyl radicals OH^- and O_2^- super oxide radical anions cannot penetrate into the cell membrane and must remain in contact with the outer surface of the bacteria [24,25]. But the active anionic molecules are effective toxic to bacterial substance. In addition, the damage of cell membrane might directly lead to the leakage of minerals, proteins and genetic materials causing ultimate cell death [26,27].

The mechanism involved in the generation of reactive oxygen species from C-CeO_2 and G-CeO_2 nanoparticles induced by UV light are shown in Figure 16.

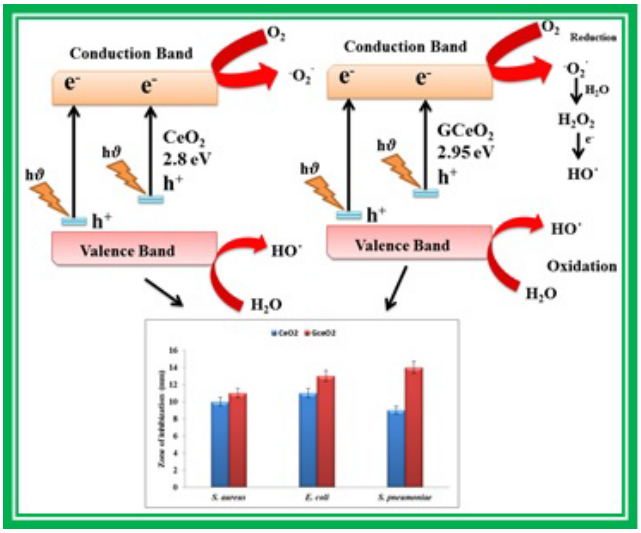

Figure 16: The mechanism involving in the generation of reactive oxygen species from C-CeO_2 and G-CeO_2 NPs induced by UV light.

$$CeO_2 + h\upsilon CeO_2(e^-) + CeO_2(h^+),\ CeO_2(h^+) + H_2O CeO_2 + {}^{\cdot}OH^- + H^+,$$
$$CeO_2(h^+) + OH^- CeO_2 + OH,\ CeO_2(e^-) + O_2 CeO_2 + {}^{\cdot}O_2^-,\ {}^{\cdot}O_2^- + H^+ HO_2^{\cdot} \text{ and}$$
$$2HO_2^{\cdot} O^2 + H_2O_2$$

The smaller sized NPs indeed have higher antibacterial activity [28]. From the XRD patterns, the particle size of C-CeO_2 and G-CeO_2 are found to be 11 nm and 8 nm respectively. The particle size of G-CeO_2 NPs is decreased as compared to that of the C-CeO_2 NPs, smaller size can easily penetrate into bacterial membranes due to their large interfacial area, thus enhancing their antibacterial efficiency. During the generation of ROS, the unsaturated fatty acids in the cell membrane will be oxidized by $^{\cdot}OH$ group, and affect the fluidity of cell membranes. Consequently decreased the thickness of bacteria cell wall and caused to bacteria death.

From the UV-Vis studies, the band gaps are observed at 2.8 eV and 2.95 eV for C-CeO_2 and G-CeO_2 NPs. The band gap of G-CeO_2 NPs is increased as compared to that of the C-CeO_2 NPs. The increasing rent of band gap G-CeO_2 NPs, it is due to NPs interaction with thiol groups in proteins, resulting in inactivation of respiratory enzymes and leading to the production of more reactive oxygen species (ROS). This band gap behavior of CeO_2 NPs played a major role in the ROS mediated toxicity, which suggested that the *A. indica* leaf extract stimulated a large amount of oxygen atoms to be adsorbed onto CeO_2 surface. Generation of more ROS in the suspension result in intense oxidative stress towards the bacteria and this reason is enhancing the antibacterial response for G-CeO_2 NPs.

From the PL spectra, green emissions are observed at 521 nm and 522 nm for C-CeO_2 and G-CeO_2 NPs. This shows the increased number of oxygen vacancies in the G-CeO_2 NPs, leading to a higher number of ROS as compared to the C-CeO_2 NPs. So that reason G-CeO_2 NPs more antibacterial activity as compared to that of C-CeO_2 NPs.

Toxicity on lung cancer cells

In present investigation, the cytotoxic effect of C-CeO_2 and G-CeO_2 NPs are examined in cultured (A549) human lung cancer cell line by exposing cells for 24 h to culture medium containing the C-CeO_2 and G-CeO_2 NPs led to around 40% and 41% inhibition at the highest concentrations used in our assays at 400 ± 0.05 µg/ml and 400 ± 0.05 µg/ml respectively in Figure 17. The cancer cell viability of are decreased partially with increasing the concentration of both CeO_2 NPs. The results show the direct dose-response relationship with tested cells only at higher concentrations, but there is no significant toxicity. In literature, same trend observed for dysprosium oxide treated A549 human lung cancer cell line at the concentration range of 500 µg/ml [29].

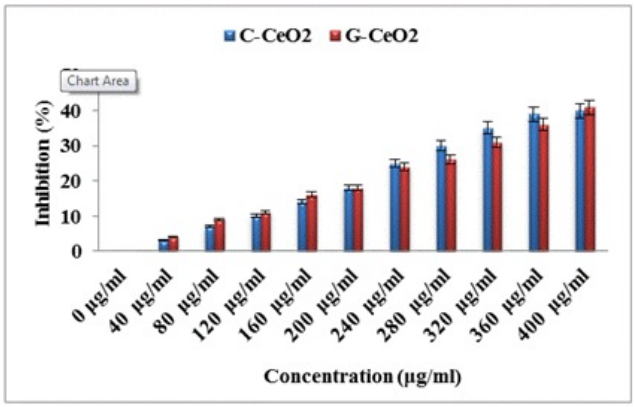

Figure 17: The effect of C-CeO_2 and G-CeO_2 NPs on the cytotoxicity property in human lung cancer cell line (A549).

The important physiognomies of apoptosis are morphological changes during cell death. Figure 18 represents that AO/EB double-stained A549 human lung cancer cell line treated with test substances 24 h underwent both early apoptosis and late apoptosis. The control or viable cells shows green fluorescence and normal cell features of uniform chromatin with an intact cell membrane, whereas, the early apoptosis cells showed bright green region with yellowish green nuclear fragmentation and membrane bubbles and apoptotic bodies outside. The late apoptosis cells exhibited orange-yellow or red nuclei with condensed or fragmented chromatin.

The results demonstrate that C-CeO_2 and G-CeO_2 NPs induce majority of viable cells shows green fluorescence and normal cell features of uniform chromatin with an intact cell membrane for 24 h treatment. Therefore, the present observation exposed the prospect for the use of synthesize C-CeO_2 and G-CeO_2 NPs are enhanced nano-carrier, due to its low toxicity.

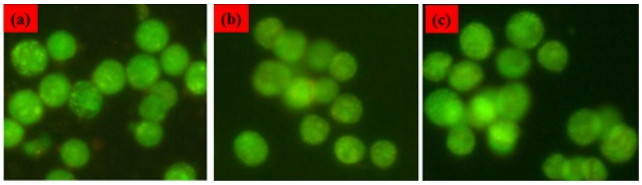

Figure 18: Cells treated with (a) control (b) C-CeO_2 and (c) G-CeO_2 NPs at the respective IC50 concentrations and the morphologies observed after staining with AO/EB.

Conclusion

In summary, CeO_2 NPs prepared chemical synthesis by co-precipitation method and green synthesis using *Azadirachta indica* leaf extract comparative studies were carried out.

From the X-ray diffraction studies confirmed that the prepared nanoparticles were face-center cubic phase. The average crystallite sizes were 11 nm and 8 nm for C-CeO_2 and G-CeO_2 NPs respectively. The XPS studies showed that from the indexed peaks corresponding to Ce (3d), C (1s) and O (1s) the respective binding energies of the elements were estimated. From the TEM and FESEM images, C-CeO_2 and G-CeO_2 NPs were nano-flake like structure and spherical structure. Elemental compositions were identified by EDAX analysis. In FT-IR spectra Ce-O stretching observed at 411 cm^{-1} and 429 cm^{-1} for C-CeO_2 and G-CeO_2 NPs respectively. From the Raman spectra, the C-CeO_2 and G-CeO_2 NPs were located at 459 and 462 cm^{-1}, these was due to the triply degenerate F2g Raman active mode of fluorite-type cubic structure i.e., asymmetric breathing mode of the oxygen atoms around the cerium ions.The UV-Vis absorption spectra, direct and indirect band gaps were observed at (2.4 eV and 2.8 eV) and (2.45 eV and 2.95 eV) for C-CeO_2 and G-CeO_2 NPs respectively. From PL spectra, red shift observed for emission of G-CeO_2 NPs values as compared to that of the C-CeO_2 NPs emission values. These were due to the formation of more organic impurity levels. The defect state was localized in between the Ce 4f and O 2p levels, leading to a red shift. These changes in the emissions were confirmed that the *A. indica* leaf extract reduced to forming the CeO_2 NPs.

The antibacterial studies performed against a set of bacterial strains showed that the G-CeO_2 NPs possessed higher antibacterial properties than the C-CeO_2 NPs. From the XRD result, the particle sizes of G-CeO_2 NPs (8 nm) decreased as compared to that of C-CeO_2 NPs (11 nm), smaller size can easily penetrate into bacterial membranes due to their large interfacial area, thus enhancing their antibacterial efficiency.

The cytotoxic effect of the C-CeO_2 and G-CeO_2 NPs were examined in cultured (A549) human lung cancer cell line by exposing cells for 24 h to culture medium containing the C-CeO_2 and G-CeO_2 NPs led to around 40% and 41% inhibition at the highest concentrations used in our assays at 400 ± 0.05 g/ml and 400± 0.05 µg/ml respectively. Therefore, the present observation exposed the prospect for the use of synthesized C-CeO_2 and G-CeO_2 NPs as enhanced nano-carrier, due to its low toxicity.

References

1. Masui T, Hirai H, Imanaka N, Adachi G, Sakata T, et al. (2002) Synthesis of cerium oxide nanoparticles by hydrothermal crystallization with citric acid. J Mater Sci Lett 21(6): 489-491.
2. Weisheng L, Huang YW, Zhou XD, Yinaf M (2006) In vitro toxicity of silica nanoparticles in human lung cancer cells. J Toxicol 25: 451-457.
3. Kopia A, Kowalski K, Chmielowska M, Leroux C (2008) Electron microscopy and spectroscopy investigations of CuOx–CeO2– δ/Si thin films. Surf Sci 602(7): 1313-1321.
4. Chaen JP, Patil S, Seal S, McGinnis JF (2006) Rare earth nanoparticles prevent retinal degeneration induced by intracellular peroxides. Nat Nanotechn 1: 142-150.
5. Niu J, Azfer A, Rogers LM, Wang X, Kolattukudy PE (2007) Cardioprotective effects of cerium oxide nanoparticles in a transgenic murine model of cardiomyopathy. Cardiovasc Res 73(3): 549-59.
6. Tarnuzzer RW, Colon J, Patil S, Seal S (2005) Vacancy engineered ceria nanostructures for protection from radiation-induced cellular damage. Nano Lett 5(12): 2573-2577.
7. Korsvik C, Patil S, Seal S, Self WT (2007) Superoxide dismutase mimetic properties exhibited by vacancy engineered ceria nanoparticles. Chem. Commun 10: 1056-1058.
8. Yadav LSR, Manjunath K, Archana B, Madhu C, Naika HR, et al. (2017) Synthesis of CeO2 nanoparticles: Photocatalytic and antibacterial activities. Eur Phys J Plus 132(5): 239.
9. Arumugam A, Karthikeyan C, Hameed AS, Gopinath K, Gowri S, et al. (2015) Synthesis of cerium oxide nanoparticles using Gloriosa superba L. leaf extract and their structural, optical and antibacterial properties. Mater Sci Eng R-Rep 49: 408-15.
10. Rahman ZS, Jairajpuri MS (1993) Neem in Unani Medicine.
11. Wright GD (2000) Resisting resistance: New chemical strategies for battling superbugs. Chem Biol, pp: R127-R137.
12. Mosmann T (1983) Rapid colorimetric assay for cellular growth and survival: application to proliferation and cytotoxicity assays. J Immunol Methods 65: 55-63.
13. Spector DL, Goldman RD, Leinwand LA (1998) Cell: A laboratory manual.
14. Yadav LSR, Manjunath K, Archana B, Madhu C, Naika HR, et al. (2016) Fruit juice extract mediated synthesis of CeO_2 nanoparticles for antibacterial and photocatalytic activities. Eur Phys J Phys, pp: 154-161.
15. Balasubramanian S, Ganesh D, Suryanarayana VVS (2014) GC-MS analysis of phyto components in the methanolic extract of Azadirachta indica. International J Pharma Biosci 5(4): 258-62.
16. Munoz-Hernández G, Escobedo-Morales A, Pal U (2008) Thermolytic growth of ZnO nanocrystals: Morphology control and optical properties. Cryst Growth Des 9(1): 297-300.
17. Gnanam S, Rajendran V (2013) Influence of various surfactants on size, morphology, and optical properties of CeO2 nanostructures via facile hydrothermal route. J Nanoparticles, pp: 1-6
18. McBride JR, Hass KC, Poindexter BD, Weber WH (1994) Raman and x-ray studies of Ce1− x RE x O2− y, where RE= La, Pr, Nd, Eu, Gd, and Tb. J Appl Phys 76(4): 2435-2441.
19. Ansari AA, Sumana G, Khan R, Malhotra BD (2009) Polyaniline-cerium oxide nanocomposite for hydrogen peroxide sensor. J Nanosci Nanotechnol 9(8): 4679-4685.
20. Tsunekawa S, Wang JT, Kawazoe Y, Kasuya A (2003) Blueshifts in the ultraviolet absorption spectra of cerium oxide nanocrystallites. J Appl Phys 94(5): 3654-3656.
21. Wang L, Ren J, Liu X, Lu G, Wang Y (2011) Evolution of SnO2 nanoparticles into 3D nanoflowers through crystal growth in aqueous solution and its optical properties. Mater Chem Phys 127(1): 114-119.
22. Morshed AH, Moussa ME, Bedair SM, Leonard R, Liu SX, et al. (1997) Violet/blue emission from epitaxial cerium oxide films on silicon substrates. Appl Phys Lett 70(13): 1647-1649.
23. Venkatesh KS, Gopinath K, Palani NS, Arumugam A, Jose SP, et al. (2016) Plant pathogenic fungus F. solani mediated biosynthesis of Nanoceria: Antibacterial and antibiofilm activity. RSC Advances 6: 42720-42729.
24. Padmavathy N, Vijayaraghavan R (2008) Enhanced bioactivity of ZnO nanoparticles—an antimicrobial study. Sci Technol Adv Mater 9(3): 035004.
25. Tam KH, Djurišić AB, Chan CM, Xi YY, Tse CW, et al. (2008) Antibacterial activity of ZnO nanorods prepared by a hydrothermal method. Thin solid films (18): 6167-6174.
26. Karunakaran C, Rajeswari V, Gomathisankar P (2010) Antibacterial and photocatalytic activities of sonochemically prepared ZnO and Ag–ZnO. J Alloys Compd 508(2): 587-591.
27. Zhang L, Jiang Y, Ding Y, Daskalakis N, Jeuken L, et al. (2010) Mechanistic investigation into antibacterial behaviour of suspensions of ZnO nanoparticles against E. coli. J Nanopart Res 12(5): 1625-1636.
28. Zhang L, Ding Y, Povey M, York D (2008) ZnO nanofluids–A potential antibacterial agent. Prog Nat Sci 18(8): 939-944.
29. Gopinath K, Chinnadurai M, Devi NP, Bhakyaraj K, Kumaraguru S, et al. (2017) One-pot synthesis of dysprosium oxide nano-sheets: Antimicrobial potential and cytotoxicity on A549 lung cancer cells. J Cluster Sci 28: 1-15.